Developing a long-term high-resolution winter fog climatology over south Asia using satellite observations from 2002 to 2020

Manoj K. Singh[a] and Ritesh Gautam[b*]

[a]School of Engineering, University of Petroleum and Energy Studies, Dehradun - 248007, India

[b]Environmental Defense Fund, Washington, DC 20009, USA

*Corresponding author – rgautam@edf.org

Abstract

The vast Indo-Gangetic Plains (IGP) south of the Himalaya are subject to dense fog every year during winter months (December-January), severely disrupting rail, air and public transport of millions of people living in northern India, Pakistan, Nepal and Bangladesh. Air pollution combined with high moisture availability in the shallow boundary layer, are important factors affecting the persistence and widespread nature of fog over the IGP. Despite the environmental significance and impacts on the public at-large, an in depth understanding of the long-term spatial-temporal distribution of the south Asian fog, is presently not available in the literature. We utilize infrared remote sensing techniques to develop a high-resolution (≈1 km x 1 km) fog detection climatology over the past two decades (2002 – 2020), using Aqua/MODIS satellite observations. A dynamic brightness temperature difference threshold (involving 3.96 μm and 11.03 μm bands) for nighttime fog detection is constructed based on systematic radiative transfer simulations involving cloud effective radius, cloud top height, cloud optical depth and satellite viewing geometry. Our satellite-based fog detection is consistent with theoretical simulations of fog characterization and is also found to be well-correlated with near-surface visibility observations of dense fog (*r* = 0.87, *p-value* << 0.01). We also provide satellite-derived nighttime estimates of fog/low-cloud effective radius which is in general agreement with the operational daytime MODIS cloud data product and limited in situ observations. In terms of fog frequency, the IGP is relatively uniformly covered by widespread fog occurrences with the largest frequency found in the low-lying Terai region, bordering India and Nepal, which is also consistently observed in our daytime fog detection results over the last two decades. Additionally, the interannual variations in fog occurrences track closely with that of relative humidity in the IGP, which is associated with shallow boundary layer conditions during winter-time favoring the formation and persistence of fog. Overall, these long-term satellite-derived results present new high-resolution data and insights into the dense and often intense winter fog occurrences which routinely engulf the entire stretch of the Indo-Gangetic Plains and cause significant degradation to ground visibility in one of the world's most densely populated regions.

1. Introduction

Each year during the winter months (December-January), the Indo-Gangetic Plains (IGP) in the northern region of south Asia, experiences widespread and persistent occurrences of dense fog. The IGP spreads across a vast stretch of agriculturally fertile belt, encompassing major parts of northern India, Pakistan, Nepal and Bangladesh, and is among the topmost densely-populated regions worldwide. The winter fog disrupts day-to-day lives of hundreds of millions of people residing in the IGP (Hameed et al., 2000; Ghude et al., 2017; Gautam and Singh, 2018; Saikawa et al., 2019). Severe spells of fog often reduce the near-surface visibility to less than 50-100 meters causing prolonged delays and cancellations in air and rail transportation, resulting in large socio-economic losses, and are even known to episodically trigger vehicular accidents (Hameed et al., 2000; Gautam et al., 2007; Jenamani, 2007; Ghude et al., 2017). In polluted environments, dense fog is also associated with significant air quality degradation making it a serious public health issue (Decesari et al., 2017; Li et al., 2016; Agarwal et al., 2017; Gupta and Elumalai, 2018), as well as impacts to agriculture (Zhang et al., 2014; Bhatta et al., 2016).

High winter-time air pollution over south Asia, in particular over the IGP, associated with anthropogenic emissions from urban, residential and industrial sources (Venkataraman et al., 2018), combined with availability of sufficient moisture in the shallow boundary layer, are some of the important factors causing the severity, persistence and widespread nature of fog over IGP (Pasricha et al., 2003; Jenamani, 2007; Pan et al., 2015; Gautam et al., 2014; Ghude et al., 2017; Dey, 2018). Owing to the importance of the winter fog in the south Asian atmospheric environment including its coupling with air pollution as well as the impacts on the densely-populated region, the understanding and characterization of fog across the IGP is critical for the purposes of fog monitoring, forecasting and assessing linkages with weather and pollution. Surface meteorological observations provide valuable information about visibility and weather related parameters needed to characterize fog episodes but these data are confined to a few point locations in the IGP and the current representation of the characteristics of fog is limited with large gaps in the context of south Asia (Gautam et al., 2007; Jenamani, 2007; Ghude et al. 2017). In this study, we utilize daily high-resolution satellite observations acquired during the past two decades, along with inputs from surface meteorological observations as well as model and observation-based reanalysis datasets, to map and quantify the spatial and temporal distribution of the dense fog cover over the IGP.

Research on fog detection using satellite remote sensing has been carried out mainly using multi-spectral systems involving thermal infrared channels (Gultepe et al., 2007). Hunt (1973) suggested that small droplets found in fog are associated with lower emissivity at 3.7 μm than at 10.8 μm, while the emissivity at these two bands is roughly the same for larger droplets. The difference in emissivity leads to significant contrast in brightness temperatures at the mid-infrared and thermal infrared bands. Further studies (e.g. Eyre et al.,1984; Turner et al., 1986; Lee et al., 1997; Ahn et al., 2003; Cermak and Bendix, 2007) applied similar approaches to satellite monitoring of nighttime fog/low stratus with observations from the Advanced Very High Resolution Radiometer (AVHRR), the Geostationary Operational Environmental Satellite Imager (GOES-8+), Geostationary Meteorological Satellite (GMS-5) and the Spinning Enhanced Visible and Infrared Imager (SEVIRI) onboard the Meteosat Second Generation (MSG) satellite. In addition, satellite-based infrared measurements combined with microwave data has also been demonstrated towards fog characterization especially for the detection of marine fog (Wilcox, 2017).

Over south Asia, there have been several efforts involving satellite remote sensing of fog using the brightness temperature difference method and retrievals of cloud microphysical properties (Gautam et al., 2007; Chaurasia et al., 2011; Ahmed et al., 2015; Dey, 2018; Gautam and Singh, 2018; Banerjee and Padmakumari, 2020). Despite recent efforts in detecting and characterizing fog over the IGP, a long-term spatial-temporal climatology of fog especially for the nighttime observations does not exist. Here, using 19 years of Moderate resolution Imaging Spectroradiometer (MODIS) satellite observations from 2002 to 2020, we produce a high-resolution climatological distribution of fog covering the entire IGP at ≈1 km x 1 km spatial resolution. Our study focuses on the nighttime fog while also providing a long-term climatology of daytime fog frequency using Terra/MODIS data. In addition, we estimate Cloud Effective Radius (CER) for the winter-time fog/low-cloud cover and discuss its characteristics over the IGP. This work is carried out using a series of systematic radiative transfer simulations involving daily nighttime radiance observations from Aqua/MODIS at ~1:30 am local-time from 2002 to 2020. We also discuss the year-to-year variability in fog during the last two decades based on our satellite-derived results, in conjunction with analysis of meteorological variables to explain the fog variability across the IGP.

2. Datasets

We used Level-1b nighttime radiance and Level-2 cloud retrievals from MODIS observations for December-January months during the 19-year period 2002 to 2020. For nighttime fog detection, both the Level-1b data and cloud products retrieved from MODIS onboard Aqua are used over the IGP bounded by 70°E - 95°E, 20°N - 33°N. The Aqua satellite follows a descending night track, crossing the equator at approximately 2100 UTC (01:30 am local time). The MODIS instrument has a swath width of 2330 km which covers the globe every 1-2 days and provides multispectral imagery in 36 discrete bands from 0.4 μm to 14.4 μm. For the nighttime fog detection algorithm, we used the emissive channels - band 22 (3.939 μm – 3.989 μm) and 31 (10.780 μm – 11.280 μm) at ≈1 km x 1 km spatial resolution (at nadir). The emissive bands are given in radiances (in the units of $W/m^2/\mu m/sr$), which were converted to equivalent black body temperature or the brightness temperature by using the Planck's law.

In addition to nighttime radiance data, we used Level-2 retrievals including Cloud Top Height (CTH), representing the geopotential height at cloud top pressure level, which is derived using infrared channel radiances. Cloud microphysical and optical properties such as Cloud Optical Thickness (COT) and CER, derived using visible radiances, were also used for daytime fog characterization. This product include datasets at a spatial resolution of 1 km or 5 km. The CER retrieval is obtained via a dual-channel retrieval method with band 7 (2.1 μm) combined with any one of the following visible-near infrared channels, band 1 (0.65 μm), band 2 (0.86 μm) or band 5 (1.2 μm). In this study, all Level-2 cloud retrievals are used from MODIS Collection 6 data product where only high confidence quality assured cloud optical properties data are reported (Platnick et al., 2016). For characterizing the impact of sensor viewing geometry on fog detection, we used the MODIS sensor zenith angle. In addition for comparative analysis of the nighttime simulated CER, we used the daytime CER which is available at a spatial resolution of 1 km.

We also used surface-based meteorological data for intercomparing with the outputs of the satellite-based fog detection algorithm. Specifically, the winter-time fog frequency is compared with the visibility data obtained from the National Climate Data Center (NCDC). The near-surface visibility data is part of the Integrated Surface Data (ISD), which includes worldwide weather observations from over 20,000 ground stations. We note here that the inter-comparison should not be considered as an ideal evaluation between satellite and surface-detected fog due to some inherent factors involving satellite-based fog detection such as orbital gaps in satellite data as well as the presence of overlaying clouds in the mid-high troposphere, affecting the MODIS retrievals of low-lying fog.

3. Nighttime fog remote sensing

We primarily discuss here the nighttime fog detection framework using MODIS observations over the IGP. In addition, we leverage an existing approach for daytime fog detection and present the fog characterization for both day and nighttime. In this section, we discuss a physically-consistent radiative transfer based approach to detect fog/low stratus cloud during nighttime, for the period 2002-2020 and apply it to the entire IGP towards developing a long-term spatial-temporal climatology. The algorithm uses a dynamic threshold based on Brightness Temperature Difference (BTD) instead of using a static threshold discussed in some previous studies over India (Chaurasia et al., 2011; Ahmed et al., 2015; Dey, 2018).

We used a bi-spectral difference method which utilizes contrasting responses to fog by two channels in the thermal bands (e.g. Ahn et al., 2003). The MODIS band 31 in the thermal IR range (11.02 μm) with an emissivity close to one for the fog (Eyre et al., 1984; Dey, 2018), is associated with a higher emissivity for fog than the shortwave infrared band 22 (3.96 μm). Fig. 1 shows three cases of widespread fog over the IGP on 30 January 2014 (Fig. 1a), 11 December 2016 (Fig. 1b) and 1 January 2018 (Fig. 1c). Corresponding to these three cases, Fig. 2 shows characteristic variations in brightness temperature (T_b), with the $T_b(band\ 31)$ on 30 January 2014 (Fig. 2a), 11 December 2016 (Fig. 2b) and 1 January 2018 (Fig. 2c) higher compared to $T_b(band\ 22)$ for the respective dates (Fig. 2d, 2e, 2f) from Aqua/MODIS observations at ~1:30 am local-time. The enhanced positive values in the brightness temperature difference $\Delta T_b = T_b(band\ 31) - T_b(band\ 22)$ observed in Fig. 2g, 2h, 2i are evident across the IGP associated with the fog (> $2K\ \Delta T_b$). This characteristic positive difference is largely associated with a reduced brightness temperature signal for band 22, which is most pronounced for fog/low-level stratus clouds with small droplets.

On the contrary, ice clouds such as the high-altitude cirrus have a reversed difference due to the increased emissivity at band 22. In cloud-free conditions, the difference is much smaller and mainly due to variations in water vapour absorption between the two bands (e.g. Ellrod et al., 1995). Additionally, the BTD method is also able to effectively distinguish fog from snow-covered areas (such as the Himalayan snow and ice cover) during nighttime, where the differences in the two spectral channels are insignificant, since snow emits more efficiently at the 3.9 µm channel than fog, similar to a clear surface or sea (Ahn et al., 2003).

In principle, positive ΔT_b values indicate the presence of fog/low-level clouds; whereas negative ΔT_b is typically associated with the presence of high clouds and $\Delta T_b \approx 0$ (or negligible difference) indicates cloud-free conditions (Eyre et al., 1984). The value of ΔT_b varies with differences in the characteristics of cloud droplets in the atmosphere. In addition, ΔT_b also varies as a function of satellite sensor zenith angle (θ) (Cermak and Bendix, 2007). We also note here that ΔT_b can be sensitive to changes in cloud top height (h_c), with infrared (IR) and shortwave IR brightness temperatures varying for clouds closer to ground vs. cloud fields that are elevated in the troposphere.

For characterizing the relationship between CER and the corresponding brightness temperature, we used a combined approach based on satellite data and theoretical simualtions using a radiative transfer model: Santa Barbara Disort Atmospheric Radiative Transfer (SBDART), which is based on a collection of sophisticated and reliable physical models, developed and widely used by the atmospheric science community over the past decades (Ricchiazzi et al., 1999). Here, we simulate nighttime radiance at the top of atmosphere (TOA), which were converted to their respective brightness temperature by inverting the Plank's function.

3.1 Characterizing infrared brightness temperatures for fog detection

In order to characterize changes in cloud droplet size and its impact on at-sensor satellite radiance/brightness temperatures, the simulated T_b values at $\theta = 20°$ for 3.96 μm and 11.02 μm, with respect to cloud effective radius are shown in Fig. 3. The Fig. 3a shows that at 11.02 μm, the T_b is not sensitive to changes in CER (symbolized here as r_c), as brightness temperature values are nearly constant across values of CER (the T_b ranges between $281 - 282$ K for $2 \leq r_c \leq 40\ \mu m$). At 3.96 μm, the T_b is highly sensitive to the changes in r_c. For smaller droplet radii (< 15 μm), T_b increases significantly from 274 K to 280 K, but for higher values of r_c (from 15 μm to 40 μm), the T_b becomes largely insensitive (varying from 280 K to 281 K) to changes in r_c. Fig. 3b shows that the difference between T_b at 11.02 μm and 3.96 μm yields greater positive values for lower r_c, whereas for higher r_c, the absolute value of ΔT_b is very small compared to that of ΔT_b at lower r_c. For instance, there is an order of magnitude difference in the ΔT_b values between $r_c = 2\ \mu m$ and $r_c = 20\ \mu m$.

Previous studies have suggested that majority of fog/low stratus clouds are associated with small cloud effective radius (e.g. r_c < 9 μm) (Bendix et al., 2005; Gautam et al., 2007; Ghude et al., 2017). The simulated ΔT_b corresponding to r_c < 9 μm were found to be larger than 2.5 K (Fig. 3b). A fixed ΔT_b threshold is presently being used by the Indian Meteorological Department (e.g. Chaurasia et al., 2011; Dey, 2018) for fog detection over India. However, our sensitivity analysis of the brightness temperature (Fig. 3) with radiative transfer computations shows that the ΔT_b threshold varies significantly as a function of the τ_c, h_c and θ along with the r_c, and therefore should not be considered as a constant value such as the fixed 2.5 K threshold considered in previous studies (Chaurasia et al., 2011).

We now demonstrate the sensitivity of T_b (and ΔT_b) to the various aforementioned cloud properties and satellite viewing geometry through a number of systematic radiative transfer computations. Fig. 4a shows the variation in T_b with r_c ($2 \leq r_c \leq 40\ \mu m$) and τ_c (τ_c= 5, 10, 20, 30) at 3.96 μm and 11.03 μm. The T_b at smaller τ_c is greater than the T_b at higher τ_c at both the SWIR and IR channels, due to the attenuation of the nighttime radiance as the opacity of the cloud increases. Fig. 4b shows T_b as a function of r_c and h_c with $2 \leq r_c \leq 40\ \mu m$ and $h_c$varying from 1 km to 4 km. The top of the fog layer at higher altitudes is cooler than at lower altitudes, which is evident in the lower brightness temperature at $h_c = 4$ km than at $h_c = 1$ km, for both 3.96 μm and 11.03 μm. There is also a small but non-negligible variation present in ΔT_b corresponding to h_c for r_c < 9 μm (Fig. 4e). In addition, we find that the ΔT_b is smaller than 2 K for fog layers with higher cloud tops and low cloud optical depth (for r_c > 9 μm), further indicating that low ΔT_b is plausible with cloud layer at high altitudes and larger r_c. Finally, the largest sensitivity is found for the satellite viewing geometry where Fig. 4c shows the variation in the T_b with θ ($0° \leq \theta \leq 60°$). The brightness temperature at both the channels, 3.96 μm and 11.02 μm, especially at the shorter wavelength, drops significantly at larger θ, where the distance between the sensor and the fog/low-cloud feature is greater than that at smaller θ. Specifically, the emitted radiation from the surface-fog feature passes through a longer atmospheric path at larger θ, which leads the brightness temperature to be cooler, compared to lower temperature at smaller θ. There is a pronounced variation in ΔT_b with θ; for example at 9 μm, the ΔT_b is 4.5 K at θ = 40°, significantly larger than ΔT_b of 2.5 K at θ = 20° (Fig. 4f). Overall, constraining the detection of foggy/low-cloud features is dependent on several key variables including cloud effective radius, cloud optical thickness, cloud top height and sensor viewing geometry, as shown here in the systematic radiative transfer simulations, underscoring the need for a dynamic threshold of ΔT_b towards enabling a robust fog detection framework.

Next, we characterize the dynamic threshold towards fog detection in satellite observations against physically-consistent radiative transfer (RT) simulations. Fig. 5a shows the brightness temperatures at 3.96 µm and 11.03 µm computed as a function of θ for different cloud top heights ($h_c = 1\ km$ and $h_c = 2\ km$) for $r_c = 9\ \mu m$. As noted earlier, the T_b at $h_c = 2\ km$ is lower than at $h_c = 1\ km$, with the T_b decreasing at larger θ (particularly after sensor zenith angle of 40°) for both the channels. Consequently, the ΔT_b increases at larger θ (Fig. 5b) for both the $h_c = 1\ km$ and $2\ km$, and follows approximately a third order polynomial. We extracted a T_b profile during a nighttime fog-covered scene from MODIS observations on 30 January 2014 (Fig. 5c), to characterize the variations in T_b as a function of θ (from 7° to 62°) and demonstrate the satellite-derived dynamic threshold for fog detection. The observed T_b profile (Fig. 5c) shows a similar variation as compared to the RT simulations with steep decline in T_b for oblique viewing geometry (θ > 40°). Fig. 5d shows that the observed foggy pixels along the transect (supplementary Fig. S1) are associated with systematically increasing ΔT_b, which are greater than the theoretical threshold. Overall, the consistency between satellite observations and RT simulations reinforces the significance of the need for a dynamical threshold for fog detection.

4. Long-term winter fog climatology over south Asia (2002-2020)

Using the aforementioned approach, we apply the nighttime detection algorithm to process daily fog maps from 2002 to 2020 over the IGP during the winter months of December and January. Fig. 6 shows spatial distribution of nighttime fog episodes covering majority of the IGP for 30 January 2014, 11 December 2016 and 1 January 2018, using Aqua/MODIS observations. The maps were created at 0.01° x 0.01° spatial resolution (approximately 1 km x 1 km resolution). We also provide here an estimation of the CER for fog-detected pixels (relevant information is provided in supplementary material). In Fig. 6b and 6c, the spatial distribution of our nighttime estimated CER along with the operationally-retrieved daytime CER from Terra/MODIS are shown for foggy pixels on 30 January 2014, 11 December 2016 and 1 January 2018, respectively. A large fraction of CER less than 9 µm (as also shown in Fig. S2 in supplementary material) suggest the effectiveness of the fog CER estimation during nighttime where the distribution is generally found to be consistent with the daytime CER.

We then expanded the processing of daily nighttime fog detection to develop a long-term climatological distribution over the IGP, for the 19-year period 2002-2020. Fig. 7a shows the mean seasonal (December-January) fog frequency from 2002-03 to 2020-21. Across the IGP, the mean fog frequency varies between 5-20 days, with about 20% of the winter nighttime observations associated with fog/low cloud cover. The largest occurrences of fog are found in the vicinity of the Himalayan foothills along the bordering areas of India and Nepal (as indicated by red shading in Fig. 7a). This observation of enhanced fog frequency is consistent with daytime observations of increased fog occurrences in the IGP near the Himalayan foothill as previously reported by Gautam et al. 2007, which represents the *Terai* region (or the lowland areas of northern India and southern Nepal).

We also observe this enhanced fog pattern in the overlapping MODIS daytime climatological distribution over the same time period from 2002-03 to 2020-21 using data from Terra observations at ~10:30 am local-time (Fig. 7b). The *Terai* region is widely known in the northern regions of south Asia for its '*seet lahar*' phenomena where long periods of cold conditions with low temperatures and calm winds persisting during the winter period, promoting the persistence of fog conditions, together with frequent low-level temperature inversion and high relative humidity (Gautam et al., 2007; Ghude et al., 2017; Saikawa et al., 2019).

For the purposes of intercomparison and validation of our nighttime detection framework, we use surface visibility data over 9 stations, as shown in supplementary Table S1, spread across the IGP, namely Amritsar, Bareilly, Gaya, Gorakhpur, Hissar, Indira Gandhi International (IGI) airport, Lucknow, Patna, and Safdarjung. Fig. 8 shows a scatter plot between poor visibility frequency (visibility < 250 m) derived from the surface meteorological data and fog frequency obtained from the nighttime satellite data analysis. The poor visibility frequency in a winter season at each station is computed by taking sum of the number of days when visibility is < 250 m at 2:30 am local-time, out of the total number of days in December-January, i.e. 62. The 2:30 am time stamp in the surface observations was the closest to the nighttime Aqua observations at ~1:30 am local-time. For each ground station, the corresponding satellite-derived seasonal fog frequency is computed as the sum of the fog-detected data averaged for 3 x 3 pixels (approximately 9 sq. km area) centered over the ground meteorological station. The slope of the regression line as indicated in Fig. 8 is 0.86 with a correlation coefficient of 0.87 (*p-value* << 0.01), suggesting that the frequency in satellite-detected closely follows a statistically significant relationship with fog-laden poor visibility conditions observed at surface. The correlation coefficient reduces to 0.84 (*p-value* << 0.01), when the visibility criteria is relaxed to less than 500 m, suggesting that the satellite-based detection is rather indicative of dense fog resulting in enhanced degradation of surface visibility (as indicated by higher correlation at poor visibility conditions of < 250 m).

In addition, the intercomparison analysis suggests slightly reduced frequency in fog occurrences in the satellite detection as compared to the surface visibility data. Our fog retrievals based on MODIS data can be limited by the mid-high level clouds in the troposphere overlaying and obscuring the fog layer closer to the ground. Furthermore, the orbital gaps also narrowly reduce the data availability from the MODIS observations contributing to a low bias in the fog frequency retrieved using satellite data. That said, the present intercomparison should not be strictly considered as validation since the surface visibility refers to horizontal visibility while the satellite-derived results correspond to atmospheric column. Overall, the close association between satellite and surface data enhance confidence in our methodology demonstrating the robustness of a high-resolution satellite data record covering the entire IGP in space and time.

We also analyzed the interannual variations in satellite-derived fog frequency with ground-observed poor visibility conditions associated with fog (visibility < 250 m) averaged over the 9 meteorological stations, and found a significantly high correlation of 0.93 (*p-value* << 0.01) (Fig. 9). The year-to-year variations in fog are found to be well correlated with monthly mean Relative Humidity (RH) (correlation coefficient of 0.77; *p-value* << 0.05), with generally lower RH associated with lower fog occurrences and vice versa. It is well known that high RH conditions prevailing in the shallow boundary layer in the winter months favor the formation fog in the IGP (Gautam et al., 2007; Ghude et al., 2017).

5. Summary

In this study, we use 19 years of satellite observations to produce a high-resolution (≈1 km x 1 km) climatology of winter fog over south Asia focusing on the Indo-Gangetic Plains, using nighttime and daytime MODIS observations for the period 2002-2020. The physical basis for nighttime fog detection lies in the characteristic differences in the infrared brightness temperature calculated for MODIS 3.96 μm and 11.03 μm bands, associated with the emissive properties of the two channels for fog droplets. We used a radiative transfer framework involving satellite radiances and existing retrievals of cloud properties to map and quantify fog detections. Here, we specifically constructed a dynamical threshold for fog detection based on brightness temperature differences as a function of various satellite and fog/low-cloud parameters including viewing geometry, fog effective radius, fog vertical distribution and its optical thickness. In addition to fog detection, we also characterize size of fog/low-cloud droplets in terms of their effective radius which is found to be less than 9 μm (mean=7.2 and standard deviation=1.1). To evaluate the performance of satellite-based fog analysis, the remote sensing derived results were intercompared with near-surface data of poor visibility (< 250 m visibility) based on nine meteorological observing sites across the IGP.

Our results indicate a high correlation between the disparate satellite and ground-based approaches, which were also supported by a close interannual relationship between relative humidity and fog occurrences over the last two decades, and further help shed light into the meteorological underpinnings of fog variability over the vast IGP. In addition, we processed the daytime fog climatology over the past two decades using thresholding approaches on a combination of cloud property retrievals from Terra/MODIS data. The nighttime and daytime analysis show similar spatial patterns and magnitudes of fog frequency across regions of northern India, Pakistan, Nepal and Bangladesh. We find the highest fog occurrences in the low-lying Terai region in the bordering areas of northern India and southern Nepal, which runs parallel to the lower Himalayan ranges, as consistently indicated in both the daytime and nighttime satellite derived data. We anticipate the high-resolution long-term fog data record derived from satellite observations in this study addresses a gap in the present understanding of the winter fog characteristics focused over the IGP, especially from a long-term spatial-temporal perspective. The satellite-based detection framework as discussed here can also be used to routinely map and quantify fog occurrences or help advance existing approaches towards developing a robust fog monitoring tool specifically in the IGP as well as in other geographies around the world that are subject to fog formation.

Acknowledgements

MODIS Level-1b and Level-2 used in this study were downloaded from NASA's LAADS DAAC https://ladsweb.modaps.eosdis.nasa.gov/. We thank Sarwar Rizvi, IIT Bombay for providing the initial analysis of fog remote sensing for this work and thank Piyush Patel, JPL/CalTech for helpful discussions regarding meteorological analysis related to fog variability. R.G. is thankful to Center of Studies in Resources Engineering, IIT Bombay for providing computational support towards the initial analysis for this work.

Declaration of Competing Interest

The authors have no competing interests to declare.

Figures

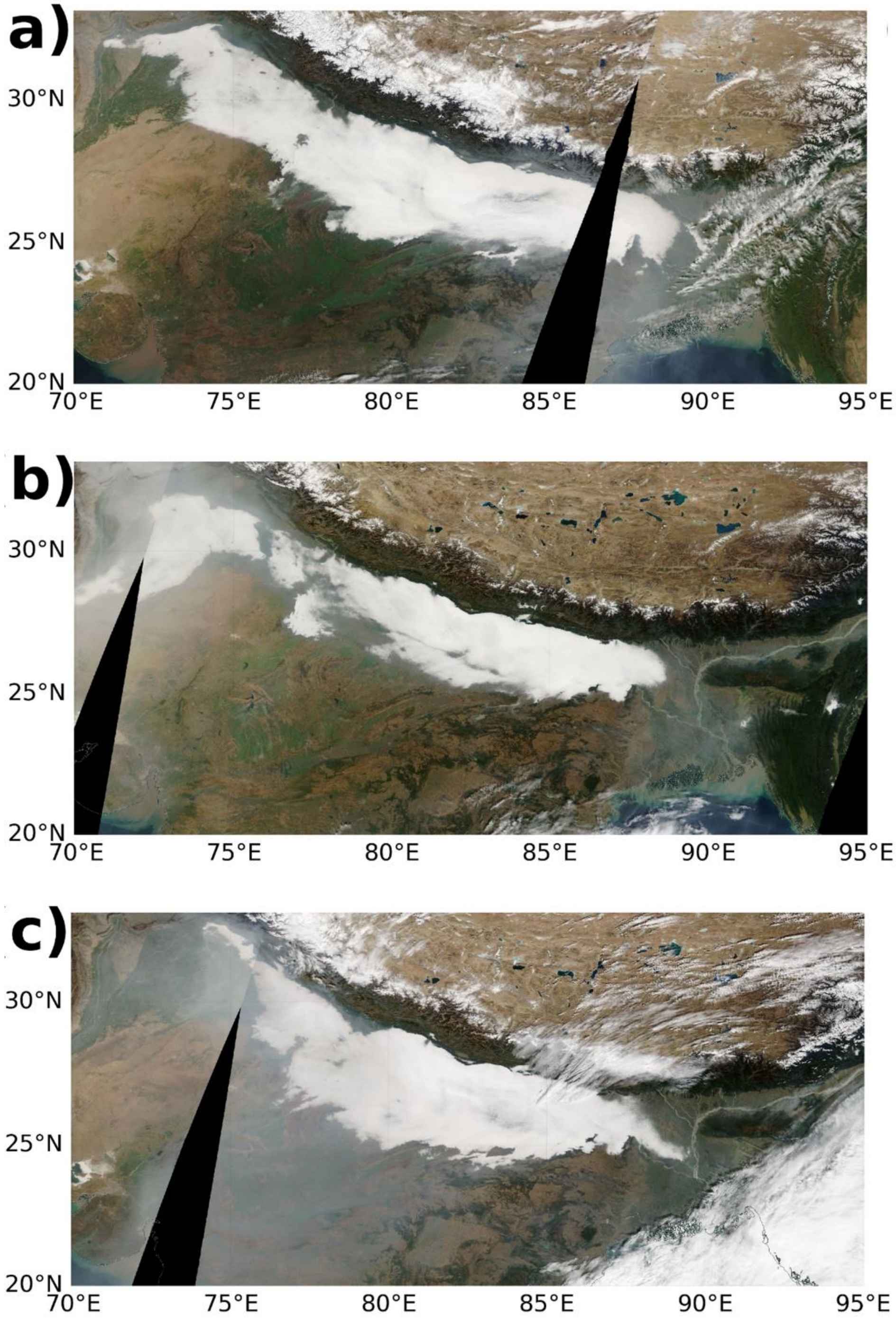

Figure 1: True color Terra/MODIS imagery of fog cover over the Indo-Gangetic Plains on (a) 30 January 2014, (b) 11 December 2016 and (c) 1 January 2018.

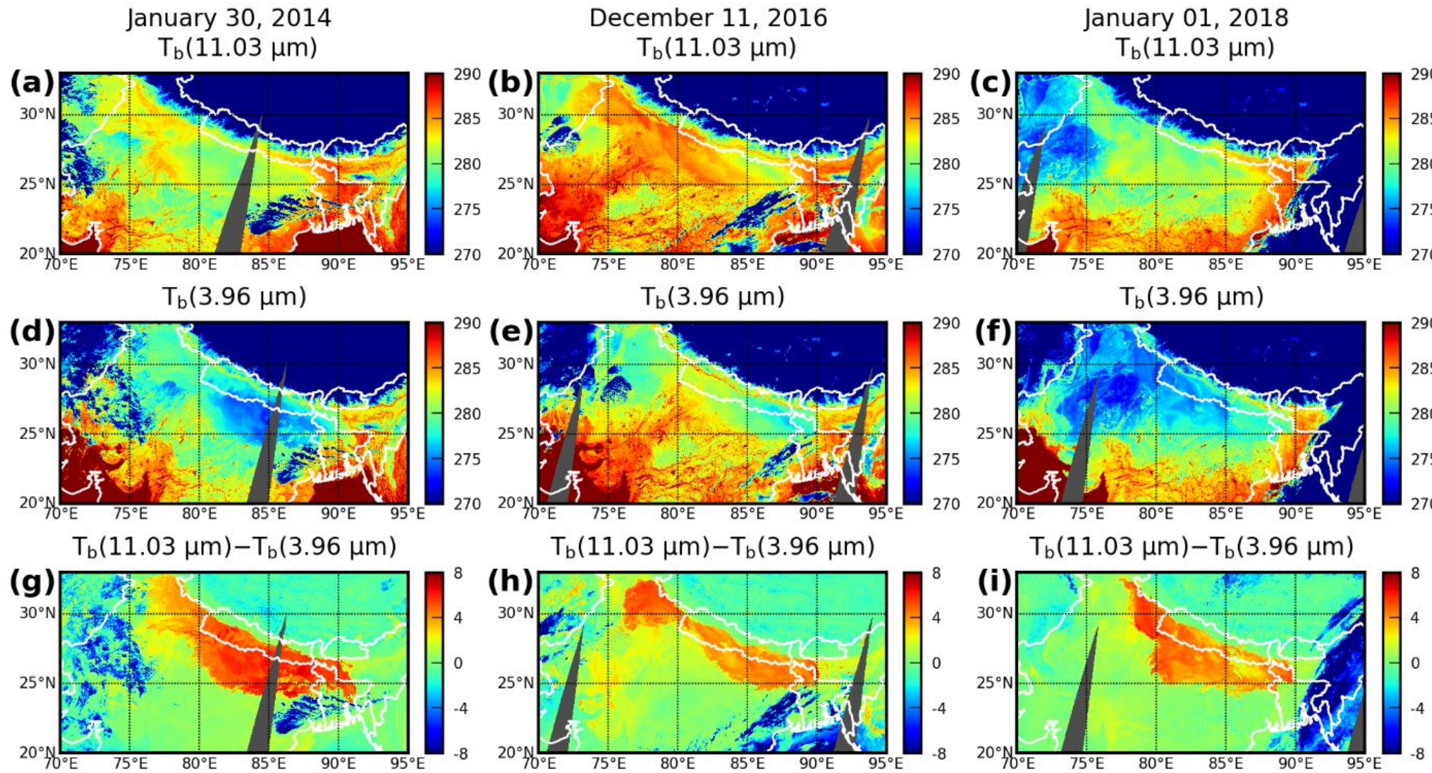

Figure 2: Brightness temperature (T_b) computed using Aqua/MODIS band 22 (3.9 μm) for (a) 30 January 2014, (b) 11 December 2016 and (c) 1 January 2018; and band 31 (11.02 μm) for (d) 30 January 2011, (e) 11 December 2016 and (f) 1 January 2018 and brightness temperature difference between band 31 and band 22 for (g) 30 January 2014 (h) 11 December 2016 (i) and 1 January 2018 from Aqua/MODIS observations focused over the Indo-Gangetic Plains bounded by 70° - 95° E longitudes and 20° - 33° N latitudes.

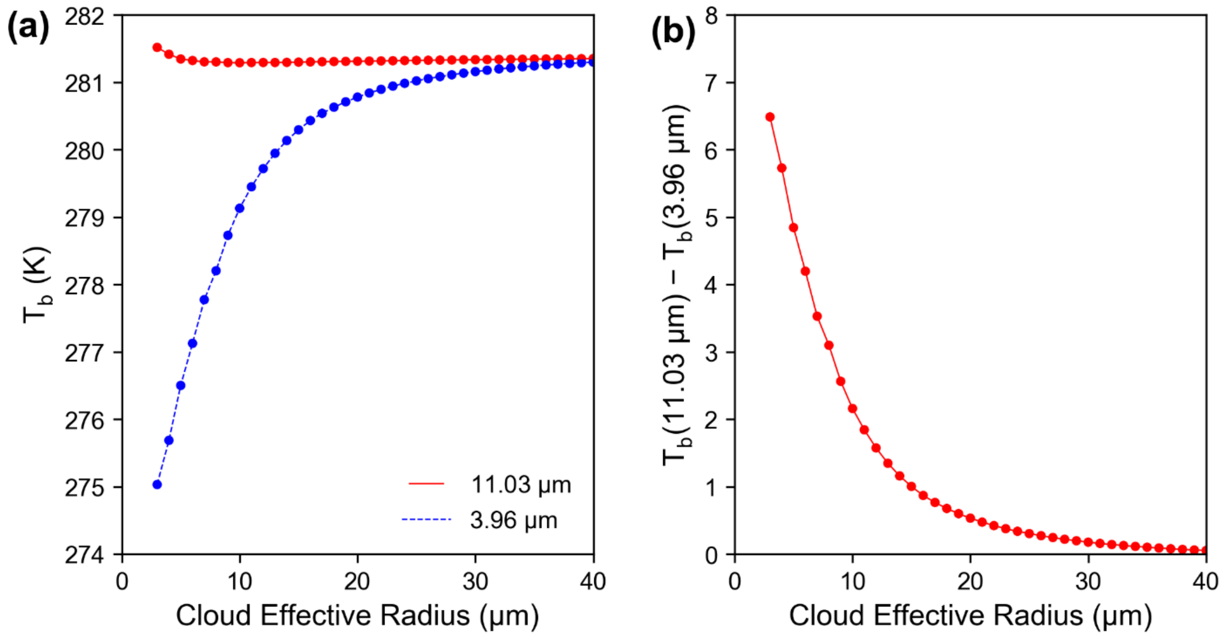

Figure 3: (a) Variation in the brightness temperature with cloud effective radius at 3.96 µm for and 11.03 µm computed from radiative transfer simulations at sensor zenith angle of 20° and cloud optical thickness of 30. (**b**) Variation of brightness temperature difference (BTD) (3.96 µm and 11.03 µm) with cloud effective radius.

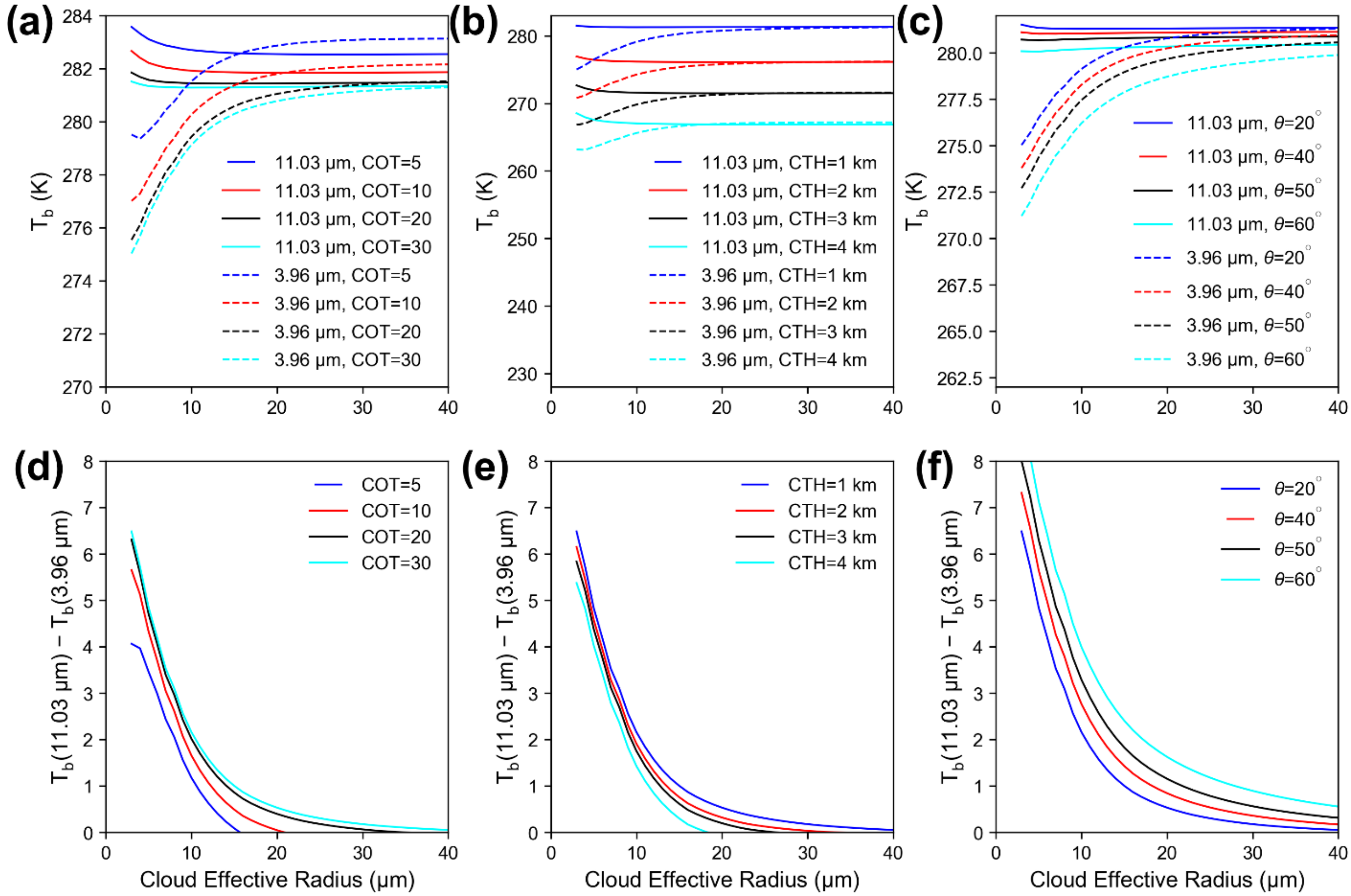

Figure 4: (a) Variation of brightness temperature (T_b) with cloud effective radius (CER) and cloud optical thickness (COT) at 3.96 μm and 11.03 μm based on radiative transfer model computations at sensor zenith angle, $\theta = 20°$ and at cloud top height (CTH) = 1 km**. (b)** Variation in $T_b(11.03\ \mu m)$ and $T_b(3.96\ \mu m)$ with CER and CTH at COT = 30 and $\theta = 20°$. **(c)** Variation of $T_b(11.03\ \mu m) - T_b(3.96\ \mu m)$ with CER and θ at COT = 30 and CTH = 1 km. **(d)** Variation of brightness temperature difference, $T_b(11.03\ \mu m) - T_b(3.96\ \mu m)$ with CER and COT at 3.96 μm and 11.03 μm at $\theta = 20°$ and at CTH = 1 km**. (e)** Variation in the $T_b(11.03\ \mu m) - T_b(3.96\ \mu m)$ with CER and CTH at COT = 30 and $\theta = 20°$. **(f)** Variation in $T_b(11.03\ \mu m) - T_b(3.96\ \mu m)$ with CER and θ at COT = 30 and CTH = 1 km.

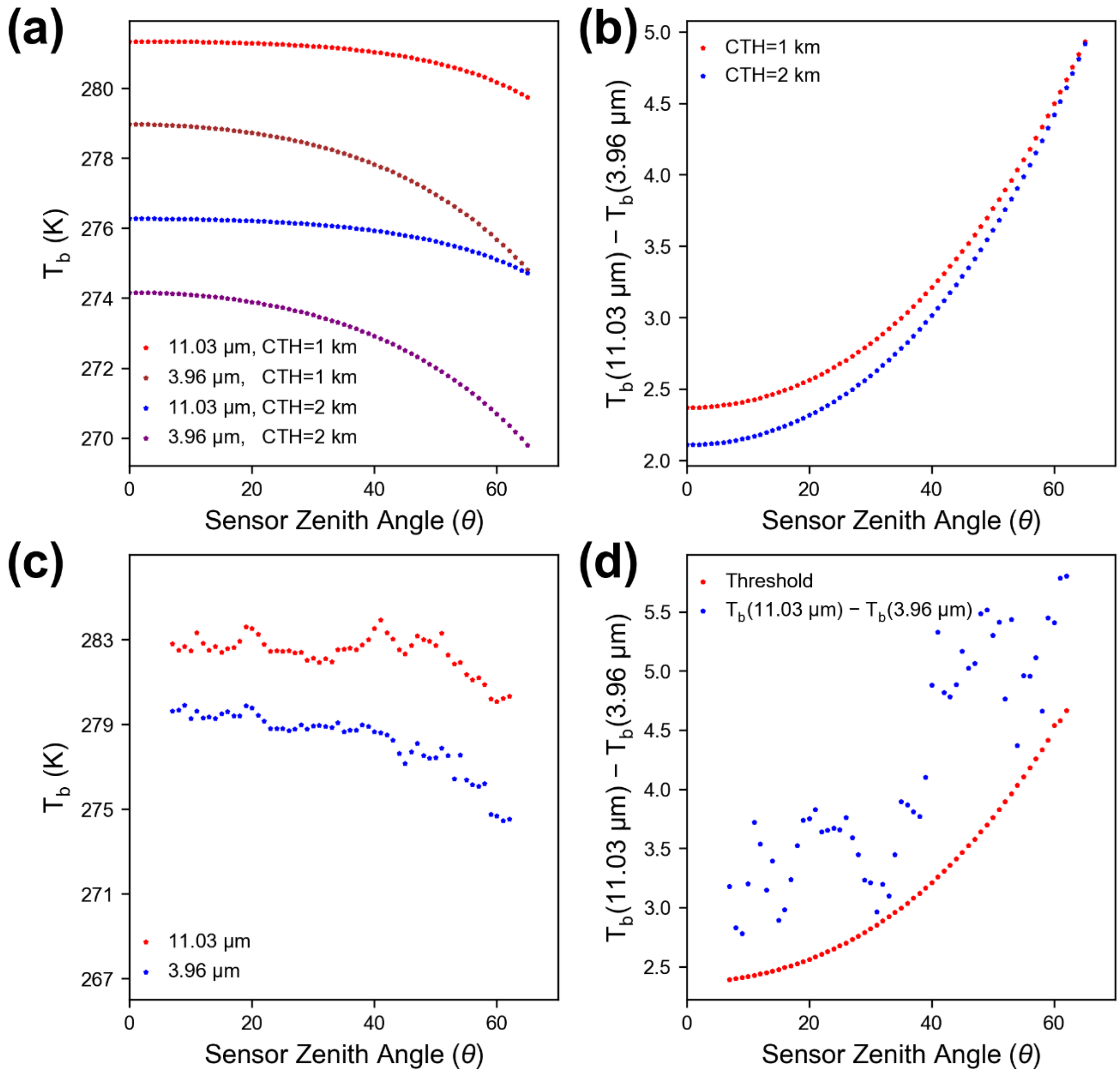

Figure 5: (**a**) Variation in the brightness temperature (T_b) with sensor zenith angle (θ) and cloud top height (CTH) at 3.96 µm and 11.03 µm and at cloud effective radius (CER = 9 µm) simulated using a radiative transfer model. (**b**) Variation of brightness temperature difference (T_b) (11.03 µm and 3.96 µm) with θ and CTH. (**c**) Variation in T_b with θ at 3.96 µm and 11.03 µm for the fog-covered pixels along a transect (the transect is a straight line joining two points, point1 (latitude=32.5°N, longitude=73.5°E) and point2 (latitude=24.5°N, longitude=85.5°E)) across the IGP for 30 January 2014. (**d**) Variation of T_b(11.03 µm) - T_b(3.96 µm) and difference threshold with θ and CTH. The red dots show the threshold computed from a radiative transfer model as a function of θ and CTH. The green dots show the brightness temperature difference along the transect for the 30 January 2014.

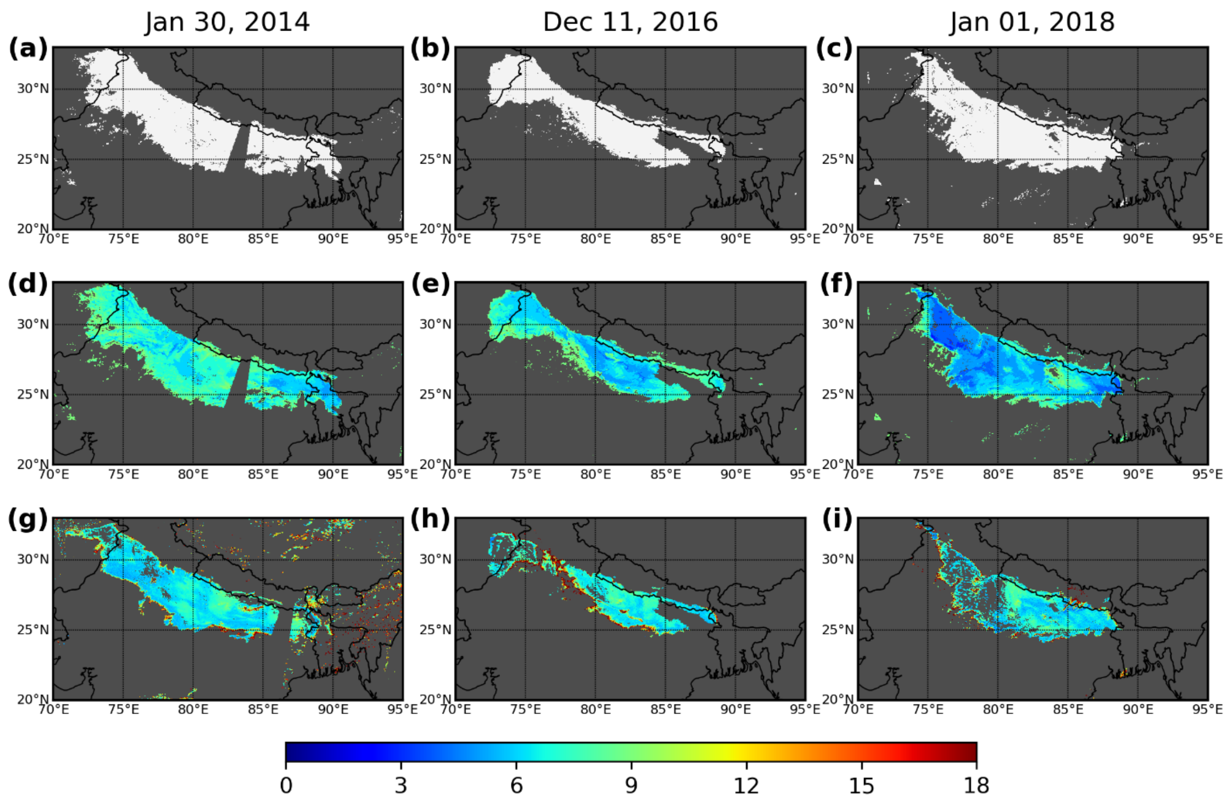

Figure 6: (a) Fog over the IGP observed using the nighttime fog detection algorithm for 30 January 2014, **(b)** 11 December 2016, and **(c)** 1 January 2018 **(d)** Simulated nighttime CER (unit - µm) over the Indo-Gangetic Plains for 30 January 2014, **(e)** 11 December 2016 and **(f)** 1 January 2018 **(g)** The CER retrievals (unit - µm)from Terra/MODIS for daytime for January 30, 2014, **(h)** 11 December, 2016 and **(i)** 1 January 2018.

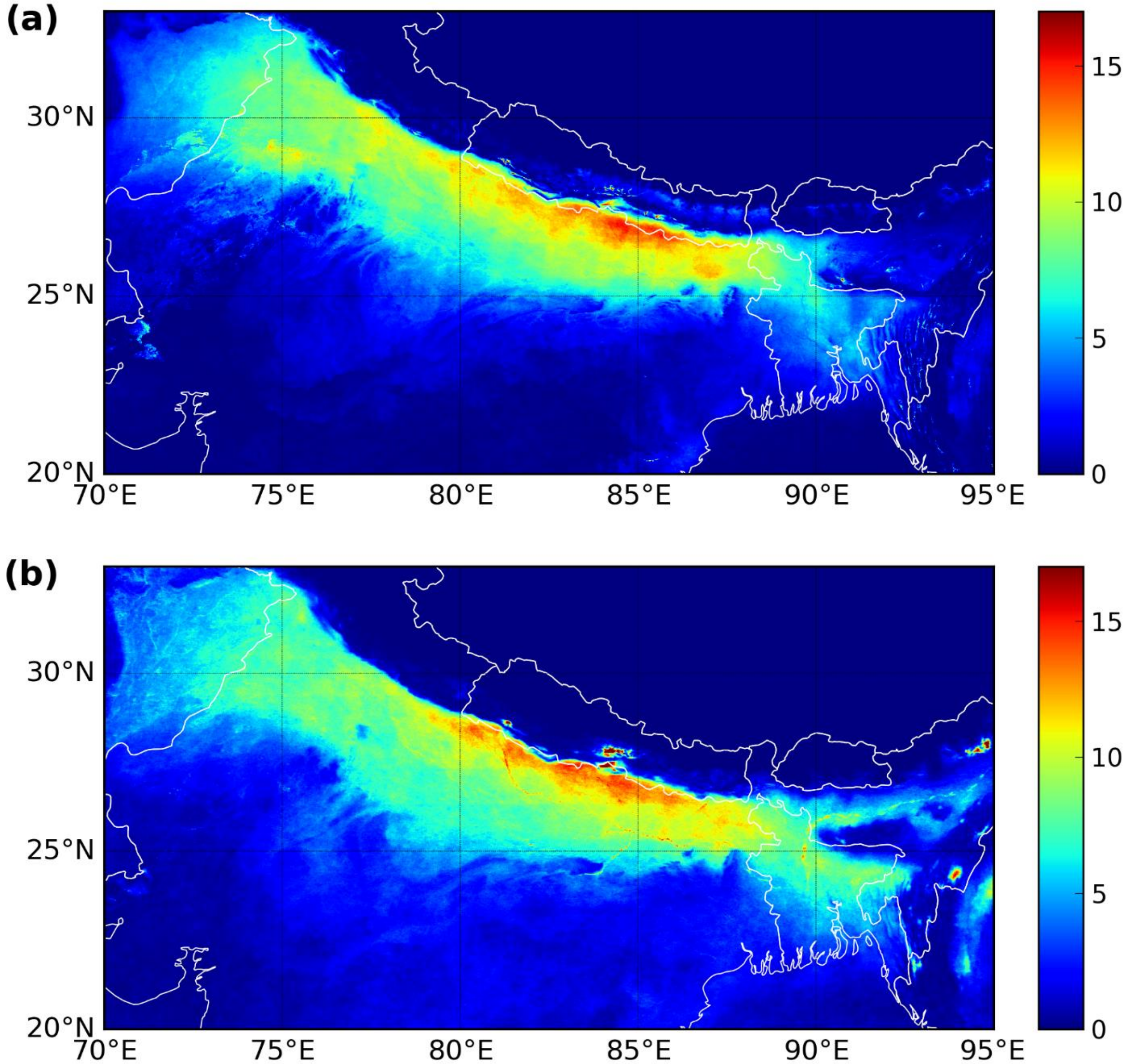

Figure 7: (a) Mean seasonal fog frequency (December-January) computed using the nighttime fog detection algorithm using daily Aqua/MODIS observations (~1:30 am local-time), over the Indo-Gangetic Plains for the period 2002-20. Colorbar indicates number of days fog was detected during December-January. **(b)** Mean seasonal fog frequency (December-January) computed using the daytime fog detection analysis using Terra/MODIS observations (~10:30 am local-time), for the period 2002-20. The largest fog frequency is found in the bordering areas of India and Nepal, along the Terai region, south of the Himalayan foothills.

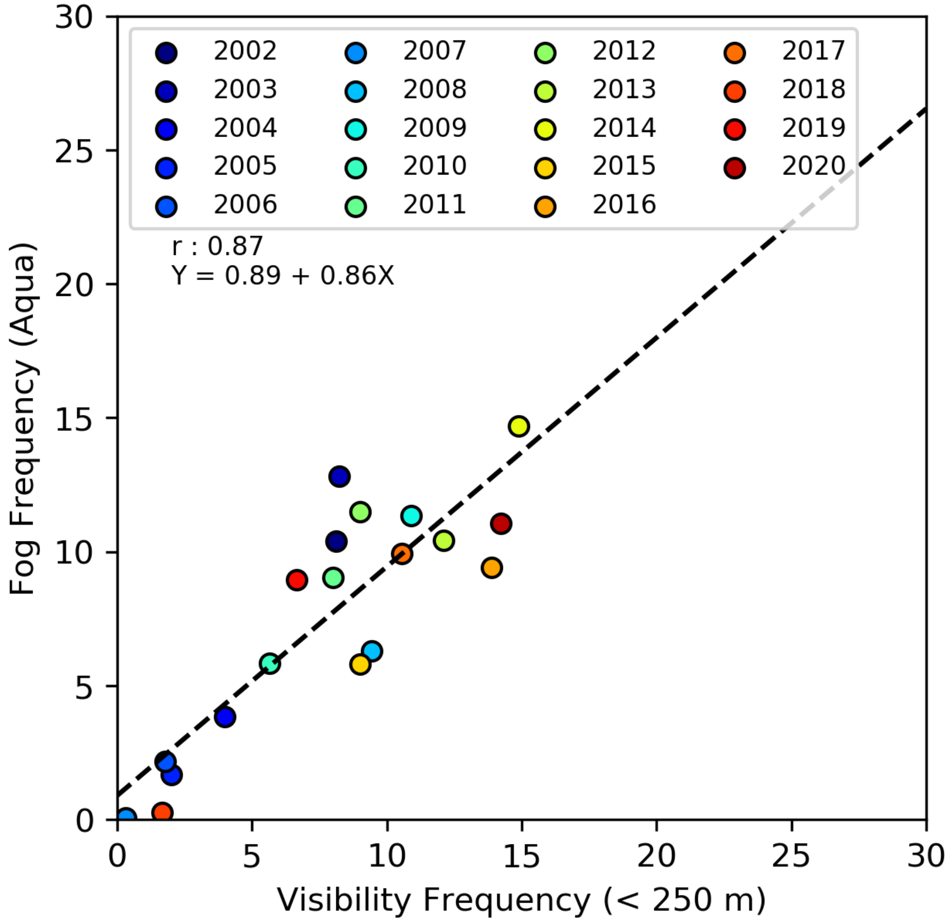

Figure 8: Intercomparison of seasonal fog frequency, derived using nighttime Aqua/MODIS observations for the period 2002-2020 for the winter months of December-January, with the poor visibility frequency (visibility < 250 m) computed from ground meteorological data.

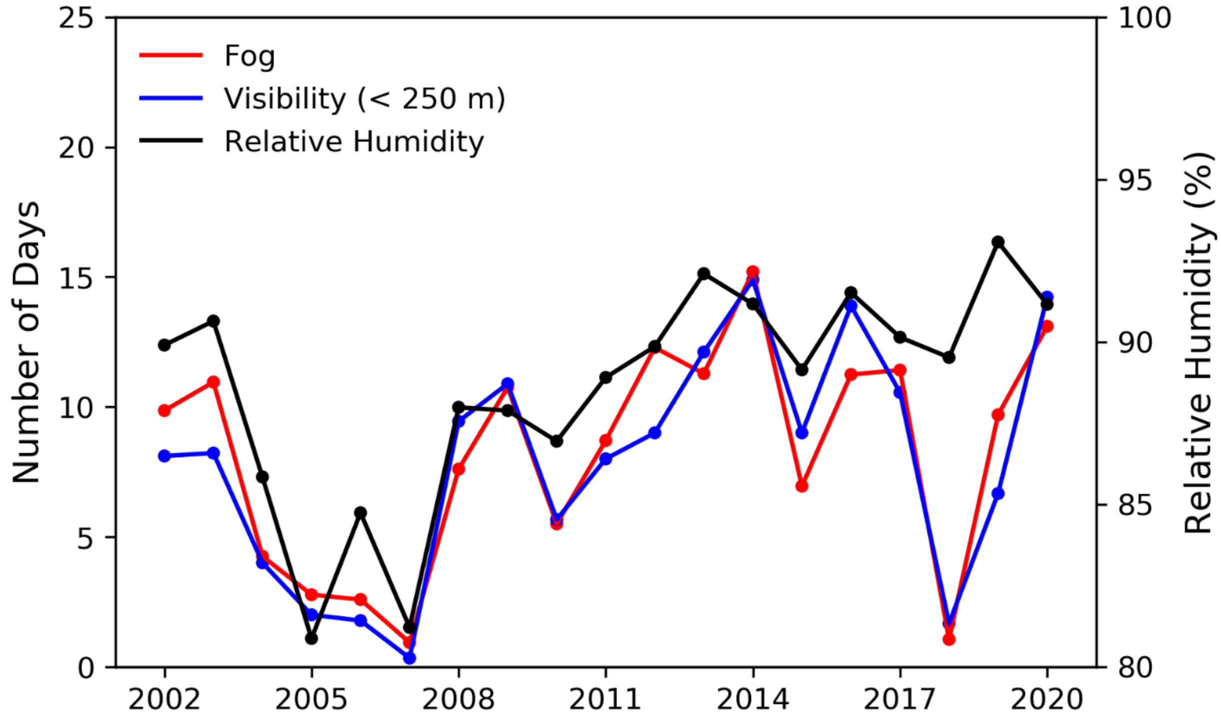

Figure 9: Interannual variations of fog frequency (red) derived using Aqua/MODIS observations for the winter months of December-January for the period 2002-2020, poor visibility frequency (visibility < 250 m) is shown in blue and relative humidity (%) from ground meteorological observations in the Indo-Gangetic Plains.

References

Agarwal, A., Mangal, A., Satsangi, A., Lakhani, A., Maharaj Kumari, K., 2017. Characterization, sources and health risk analysis of PM2. 5 bound metals during foggy and non-foggy days in sub-urban atmosphere of Agra. Atmospheric Research 197, 121–131.

Ahmed, R., Dey, S., Mohan, M., 2015. A study to improve night time fog detection in the Indo-Gangetic basin using satellite data and to investigate the connection to aerosols. Meteorological Applications 22, 689–693.

Ahn, M.H., Sohn, E.H., Hwang, B.J., 2003. A new algorithm for sea fog/stratus detection using GMS-5 IR data. Advances in Atmospheric Sciences 20, 899–913.

Banerjee, S., Padmakumari, B., 2020. Spatiotemporal variability and evolution of day and night winter fog over the Indo Gangetic Basin using INSAT-3D and comparison with surface visibility and aerosol optical depth. Science of The Total Environment 745, 140962.

Bendix, J., Thies, B., Cermak, J., Nau, T., 01 Dec. 2005. Ground fog detection from space based on MODIS daytime data–a feasibility study. Weather and Forecasting 20, 989 – 1005.

Bhatta, G.D., Aggarwal, P.K., Kristjanson, P., Shrivastava, A.K., 2016. Climatic and non-climatic factors influencing changing agricultural practices across different rainfall regimes in South Asia. Current Science 110, 1272–1281.

Cermak, J., Bendix, J., 2007. Dynamical nighttime fog/low stratus detection based on Meteosat SEVIRI data: A feasibility study. Pure and Applied Geophysics 164, 1179–1192.

Chaurasia, S., Sathiyamoorthy, V., Shukla, B., Simon, B., Joshi, P., Pal, P., 2011. Night time fog detection using MODIS data over Northern India. Meteorological Applications 18, 483 – 494.

Decesari, S., Sowlat, M. H., Hasheminassab, S., Sandrini, S., Gilardoni, S., Facchini, M. C., … Sioutas, C. (2017). Enhanced toxicity of aerosol in fog conditions in the Po Valley, Italy. Atmospheric Chemistry and Physics, 17(12), 7721– 7731.

Dey, S., 2018. On the theoretical aspects of improved fog detection and prediction in India. Atmospheric Research 202, 77–80.

Ellrod, G.P., 1995. Advances in the detection and analysis of fog at night using GOES multispectral infrared imagery. Weather and Forecasting 10, 606 – 619.

Eyre, J., Brownscombe, J., Allam, R., 1984. Detection of fog at night using Advanced Very High Resolution Radiometer (AVHRR) imagery. Meteorological Magazine 113, 266–271.

Gautam, R., Hsu, N.C., Kafatos, M., Tsay, S.C., 2007. Influences of winter haze on fog/low cloud over the Indo-Gangetic plains. Journal of Geophysical Research: Atmospheres 112.

Gautam, R., 2014. Challenges in Early Warning of the Persistent and Widespread Winter Fog over the Indo-Gangetic Plains: A Satellite Perspective. Springer Netherlands, Dordrecht. pp. 51–61.

Gautam, R., Singh, M.K., 2018. Urban heat island over Delhi punches holes in widespread fog in the Indo-Gangetic plains. Geophysical Research Letters 45, 1114–1121.

Ghude, S., Bhat, G., Prabha, T., Jenamani, R., Chate, D., Safai, P., Karipot, A., Konwar, M., Pithani, P., Sinha, V., Pasumarti, R., Dixit, S., Tiwari, S., Todekar, K., Varpe, S., Srivastava, A., Bisht, D., Murugavel, P., Ali, K., Rajeevan, M., 2017. Winter fog experiment over the Indo-Gangetic plains of India. Current Science 112, 767.

Gultepe, I., Tardif, R., Michaelides, S.C., Cermak, J., Bott, A., Bendix, J., Müller, M.D., Pagowski, M., Hansen, B., Ellrod, G. and Jacobs, W., 2007. Fog research: A review of past achievements and future perspectives. Pure and applied geophysics 164(6), 1121-1159.

Gupta, S.K., Elumalai, S.P., 2018. Adverse impacts of fog events during winter on fine particulate matter, CO and VOCs: a case study of a highway near Dhanbad, India. Weather 73, 396–402.

Hameed, S., Mirza, M.I., Ghauri, B.M., Siddiqui, Z.R., Javed, R., Khan, A.R., Rattigan, O.V., Qureshi, S., Husain, L., 2000. On the widespread winter fog in Northeastern Pakistan and India. Geophysical Research Letters 27, 1891–1894.

Hunt, G.E., 1973. Radiative properties of terrestrial clouds at visible and infra-red thermal window wavelengths. Quarterly Journal of the Royal Meteorological Society 99, 346–369.

Jenamani, R., 2007. Alarming rise in fog and pollution causing a fall in maximum temperature over Delhi. Current Science 93.

Lee, T.F., Turk, F.J., Richardson, K., 1997. Stratus and fog products using goes-89 3.9- μ m data.Weather and Forecasting 12, 664 – 677.

Li, H., Wang, Q., Shao, M., Wang, J., Wang, C., Sun, Y., Qian, X., Wu, H., Yang, M., Li, F., 2016. Fractionation of airborne particulate-bound elements in haze-fog episode and associated health risks in a megacity of southeast China. Environmental Pollution 208, 655–662.

Pan, X., Chin, M., Gautam, R., Bian, H., Kim, D., Colarco, P. R., ... & Bellouin, N., 2015. A multi-model evaluation of aerosols over South Asia: common problems and possible causes. Atmospheric Chemistry and Physics 15, 5903-5928.

Pasricha, P.K., Gera, B.S., Shastri, S., Maini, H.K., John, T., Ghosh, A.B., Tiwari, M.K., Garg, S.C., 2003. Role of the water vapour green-house effect in the forecasting of fog occurrence. Boundary-Layer Meteorology 107, 469–482.

Platnick, S., Meyer, K.G., King, M.D., Wind, G., Amarasinghe, N., Marchant, B., Arnold, G.T., Zhang, Z., Hubanks, P.A., Holz, R.E., Yang, P., Ridgway, W.L., Riedi, J., 2016. The MODIS cloud optical and microphysical products: Collection 6 updates and examples from terra and aqua. IEEE Transactions on Geoscience and Remote Sensing 55, 502–525.

Ricchiazzi, P., Yang, S., Gautier, C., Sowle, D., 01 Oct. 1998. SBDART: A research and teaching software tool for plane-parallel radiative transfer in the earth's atmosphere. Bulletin of the American Meteorological Society 79, 2101 – 2114.

Saikawa, E., Panday, A., Kang, S., Gautam, R., Zusman, E., Cong, Z., Somanathan, E., Adhikary, B., 2019. Air Pollution in the Hindu Kush Himalaya. Springer International Publishing, Cham. pp. 339–387.

Turner, J., Allam, R., Maine, D., 1986. A case-study of the detection of fog at night using channels 3 and 4 on the Advanced Very High-Resolution Radiometer (AVHRR). Meteorological Magazine 115, 285–290.

Venkataraman, C., Brauer, M., Tibrewal, K., Sadavarte, P., Ma, Q., Cohen, A., Chaliyakunnel, S., Frostad, J., Klimont, Z., Martin, R.V., Millet, D.B., Philip, S., Walker, K., Wang, S., 2018. Source influence on emission pathways and ambient PM 2.5 pollution over India (2015–2050). Atmospheric Chemistry and Physics 18, 8017–8039.

Wilcox, E. M. (2017). Multi-spectral remote sensing of sea fog with simultaneous passive infrared and microwave sensors. In Marine Fog: Challenges and Advancements in Observations, Modeling, and Forecasting. Springer, Cham 511-526.

Zhang, Y.J., Holbrook, N.M., Cao, K.F., 2014. Seasonal dynamics in photosynthesis of woody plants at the northern limit of Asian tropics: potential role of fog in maintaining tropical rainforests and agriculture in Southwest China. Tree Physiology 34, 1069–1078.

Supplementary material

Developing a long-term high-resolution winter fog climatology over south Asia using satellite observations from 2002 to 2020

Manoj K. Singh[a] and Ritesh Gautam[b*]

[a]School of Engineering, University of Petroleum and Energy Studies, Dehradun - 248007, India

[b]Environmental Defense Fund, Washington, DC 20009, USA

*Corresponding author – rgautam@edf.org

S1. Estimation of nighttime CER

We created a lookup table for brightness temperature at 11.03 µm and 3.96 µm and their difference for characterizing fog/low clouds as a function of θ, r_c, h_c and COT. Since the MODIS cloud product does not include retrievals of cloud effective radius during nighttime observations, the microphysics information is presently lacking for fog/low cloud in satellite data. We provide here an estimation of the r_c for fog-detected pixels. For instance for each value of t_c assumed between 25-35, we simulated the effective radius which was used to compute a mean r_c along with the uncertainty based on +/-1 standard deviation (SD). Fig. 6 and Fig. S2a, S2b and S2c (in supporting information) show the simulated nighttime r_c at foggy pixels for 30 January 2014, 11 December 2016 and 1 January 2018, respectively. In all three cases, the maximum SD of the retrieved r_c is 0.5; therefore, the r_c at each pixel is similar for all values of t_c between 25-35. Since nighttime cloud effective radii are not available, the simulated r_c are compared with MODIS daytime cloud effective radius, as a way of intercomparison but not validation. The Figures S2d, S2e and S2f show the MODIS daytime cloud effective radius for 30 January 2014, 11 December 2016 and 1 January 2018, respectively. The figures suggest that the CER is consistently less than 9 µm in both nighttime and daytime analysis where the histogram distributions are generally found to be consistent.

Supplementary figures:

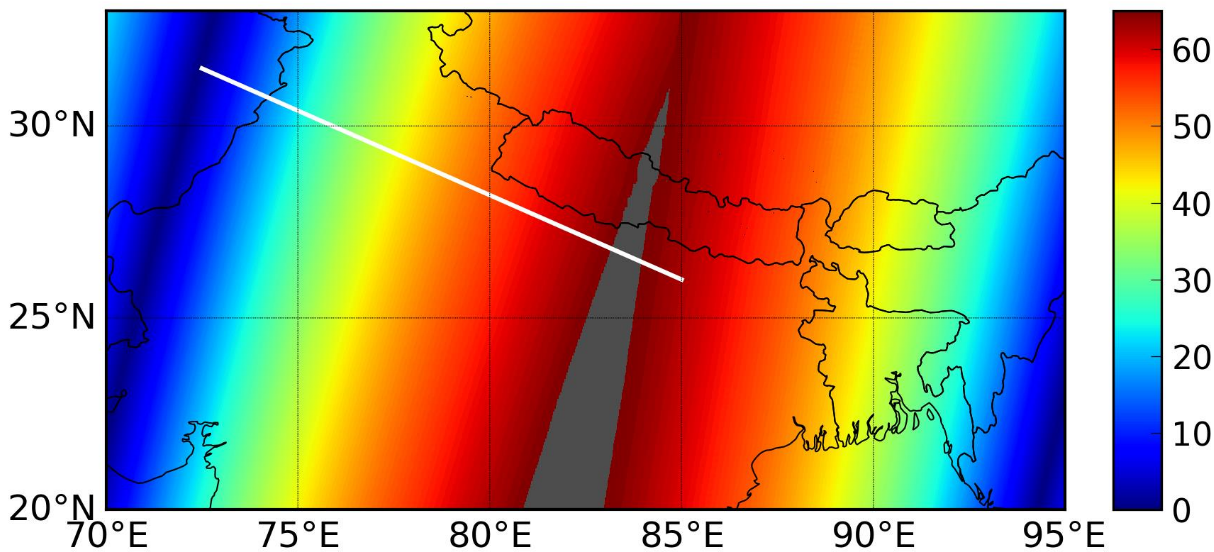

Figure S1: A transect (in white color) in the IGP along which the plots in main Fig. 5c and Fig. 5d are presented. For reference, in the background MODIS sensor zenith angle is shown (with its colorbar indicating angles in degrees) on 30 January 2014.

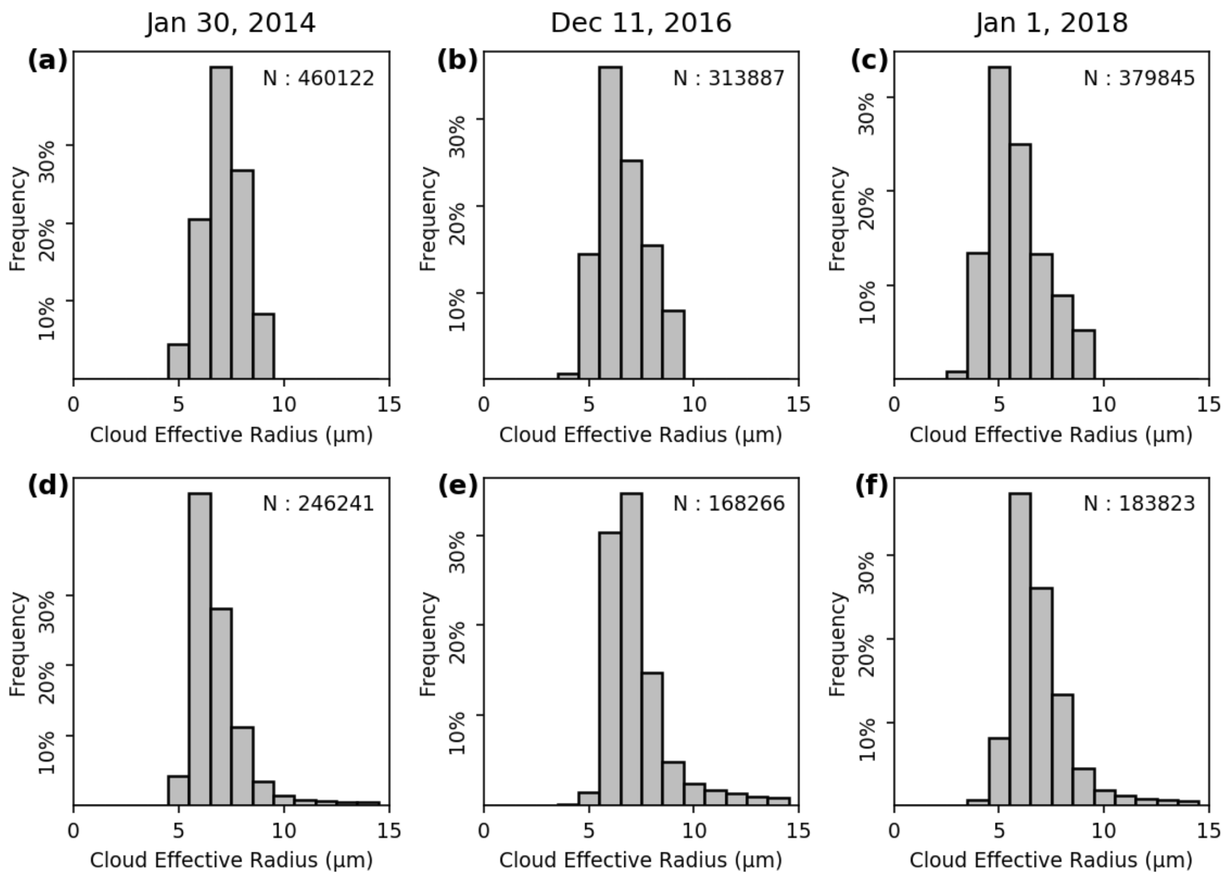

Figure S2: Histogram of the radiative transfer simulated nighttime CER over the IGP for **(a)** 30 January 2014, **(b)** 11 December 2016 and **(c)** 1 January 2018. Histograms of the CER retrievals from the MODIS (Terra) for daytime for **(d)** January 30, 2014, **(e)** 11 December, 2016 and **(f)** 1 January 2018 are also shown.

Table S1: City names and coordinates of the nine ground stations distributed across IGP.

Name	Latitude	Longitude
Amritsar	31.710° N	74.797° E
Bareilly	28.422° N	79.451° E
Gaya	24.744° N	84.951° E
Gorakhpur	26.740° N	83.450° E
Hissar	29.179° N	75.755° E
IGI	28.567° N	77.103° E
Lucknow	26.761° N	80.889° E
Patna	25.591° N	85.088° E
Safdarjung	28.585° N	77.206° E